

# Quantitative nanoscale vortex imaging using a cryogenic quantum magnetometer

L. Thiel<sup>1</sup>, D. Rohner<sup>1</sup>, M. Ganzhorn<sup>1</sup>, P. Appel<sup>1</sup>, E. Neu<sup>1</sup>, B. Müller<sup>2</sup>, R. Kleiner<sup>2</sup>, D. Koelle<sup>2</sup> and P. Maletinsky<sup>1\*</sup>

**Microscopic studies of superconductors and their vortices play a pivotal role in understanding the mechanisms underlying superconductivity<sup>1–5</sup>. Local measurements of penetration depths<sup>6</sup> or magnetic stray fields<sup>7</sup> enable access to fundamental aspects such as nanoscale variations in superfluid densities<sup>6</sup> or the order parameter symmetry of superconductors<sup>8</sup>. However, experimental tools that offer quantitative, nanoscale magnetometry and operate over large ranges of temperature and magnetic fields are still lacking. Here, we demonstrate the first operation of a cryogenic scanning quantum sensor in the form of a single nitrogen–vacancy electronic spin in diamond<sup>9–11</sup>, which is capable of overcoming these existing limitations. To demonstrate the power of our approach, we perform quantitative, nanoscale magnetic imaging of Pearl vortices in the cuprate superconductor  $\text{YBa}_2\text{Cu}_3\text{O}_{7-\delta}$ . With a sensor-to-sample distance of  $\sim 10$  nm, we observe striking deviations from the prevalent monopole approximation<sup>12</sup> in our vortex stray-field images, and find excellent quantitative agreement with Pearl's analytic model<sup>13</sup>. Our experiments provide a non-invasive and unambiguous determination of the system's local penetration depth and are readily extended to higher temperatures and magnetic fields. These results demonstrate the potential of quantitative quantum sensors in benchmarking microscopic models of complex electronic systems and open the door for further exploration of strongly correlated electron physics using scanning nitrogen–vacancy magnetometry.**

Understanding the microscopic mechanisms of superconductivity is a central topic of modern condensed-matter physics and is vital for the development of novel superconducting materials of technological and scientific relevance. A multitude of approaches have been developed in the past to study superconductivity from the microscale<sup>1,2</sup> to the nanoscale, where scanning probe technologies based on electron tunnelling<sup>3–5</sup>, scanning superconducting quantum interference devices<sup>14,15</sup> or magnetic force microscopy<sup>12</sup> have played pivotal roles. Although such approaches continue to deliver unprecedented insight into the physics of superconductors and condensed-matter systems in general, they also suffer from drawbacks such as limited temperature and magnetic field range, limited spatial resolution, high invasiveness, or the inability to address electrically isolating samples. New technologies to overcome these limitations for nanoscale studies of condensed-matter systems at low temperatures are therefore highly sought after. A particularly promising approach to nanoscale magnetic field imaging was recently enabled by the advent of nanoscale magnetometers, based on single electronic spins in diamond nitrogen–vacancy (NV) centres<sup>16–18</sup>. Such nanoscale quantum sensors have the potential to overcome the above-mentioned limitations and thus promise to deliver a highly valuable addition to the existing toolset for

nanoscale studies of complex electronic systems<sup>19</sup>. Although the combination of atomic force microscopy and optical addressing of NV spins under cryogenic conditions has recently been demonstrated<sup>20</sup>, cryogenic operation of a scanning NV magnetometer has remained an outstanding challenge, which we successfully overcome in this work.

Magnetometry with NV centre spins in diamond builds on the fact that the negatively charged NV crystal defect can be optically addressed and possesses a spin-1 ground state, with a highly spin-dependent fluorescence rate (Fig. 1a). Optical excitation at 532 nm pumps the NV into the  $|m_s = 0\rangle$  state, from which resonant microwave magnetic fields can promote it to one of the less-fluorescent  $|m_s = \pm 1\rangle$  states. In combination, these properties allow for the efficient optical detection of NV electron spin resonance (ESR)<sup>18</sup>, as shown in Fig. 1b for a single NV in our cryogenic apparatus. NV magnetometry is based on magnetic dispersion of the  $|m_s = \pm 1\rangle$  states, which leads to a linear splitting of  $2\gamma_{\text{NV}}B_{\text{NV}}$  of the two NV ESR dips, where  $\gamma_{\text{NV}} = 28 \text{ MHz mT}^{-1}$  and  $B_{\text{NV}}$  is the magnetic field along the NV symmetry axis. Magnetometry based on such direct ESR measurements yields typical sensitivities of a few  $\mu\text{T Hz}^{-1/2}$  (ref. 18), which is generally sufficient for the magnetic targets addressed in this work. For weaker magnetic sources, the sensitivity can be further enhanced by coherent spin manipulation and dynamical decoupling<sup>16</sup>, which for the type of devices used here improves the sensitivity to the nT  $\text{Hz}^{-1/2}$  range<sup>11</sup>.

The present experimental set-up (Fig. 1c) consists of a combined confocal and atomic force microscope (AFM) operating in a  $^4\text{He}$  bath cryostat with a base temperature of 4.2 K (see Methods). This approach yields a high cooling power, minimal vibrations for AFM operation, and allows for full, vectorial magnetic field control up to 0.5 T. The microscope is placed in a  $^4\text{He}$  buffer gas-filled housing, which is directly immersed in the liquid  $^4\text{He}$  bath for cooling. Optical access is provided by a quartz window on top of the cryostat and a cryogenic objective, rigidly attached to the microscope head. The single NV spin for magnetometry is embedded in an individual, all-diamond scanning probe within  $\sim 10$  nm of the tip<sup>11</sup> (Fig. 1d). This approach ensures high NV photon collection efficiencies for sensitive magnetometry, and close proximity of the NV to the sample for high-resolution imaging<sup>11,21</sup>.

Our experimental demonstration of cryogenic, nanoscale NV magnetometry was performed by imaging Pearl vortices in the prototypical superconductor  $\text{YBa}_2\text{Cu}_3\text{O}_{7-\delta}$  (YBCO) with a transition temperature of  $T_c \approx 89$  K. The type II superconductor YBCO is among the best-studied high- $T_c$  superconductors, forms a model system for strongly correlated electron physics, and hosts vortices that generate non-trivial stray magnetic fields<sup>12</sup>. It therefore offers an ideal testbed to demonstrate the applicability of our method and allows us to benchmark existing models for vortex stray fields

<sup>1</sup>Department of Physics, University of Basel, Klingelbergstrasse 82, Basel CH-4056, Switzerland. <sup>2</sup>Physikalisches Institut and Center for Quantum Science (CQ) in LISA\*, Universität Tübingen, Auf der Morgenstelle 14, D-72076 Tübingen, Germany. \*e-mail: [patrick.maletinsky@unibas.ch](mailto:patrick.maletinsky@unibas.ch)

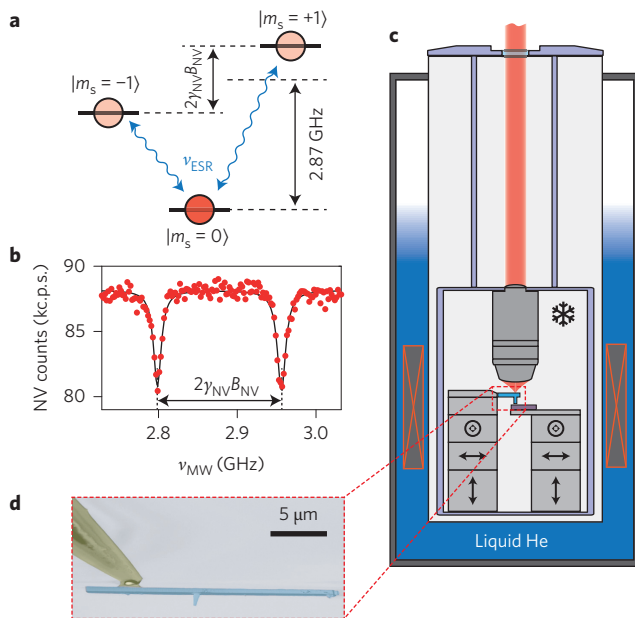


**Figure 1 | Basis of NV magnetometry and overview of experimental apparatus.** **a**, Ground-state spin levels of the negatively charged diamond NV centre, which exhibit spin-dependent fluorescence rates (red circles) and optical spin pumping under green excitation (see main text). Microwave magnetic fields of frequency  $\nu_{\text{ESR}}$  can drive ESR, which is optically detectable. **b**, Typical NV ESR trace obtained from a single NV in a diamond scanning probe at 4.2 K. Fluorescence count rate, ESR contrast and linewidth yield a magnetic field sensitivity of  $11.9 \mu\text{T Hz}^{-1/2}$ . **c**, Layout of the cryogenic, scanning NV magnetometer. Tip and sample scanning are enabled by three-axis coarse and fine positioning units, and NV fluorescence is collected through a tailor-made low-temperature objective. The microscope is kept in a liquid  $^4\text{He}$  bath at a temperature of 4.2 K. **d**, False-colour electron microscope image of an all-diamond scanning probe, as used here. The NV sensor spin is located at the apex of the nanopillar visible in the centre of the diamond cantilever.

against one another. The studied samples (Fig. 2a) consisted of a thin, single-crystalline film of YBCO (thickness  $d_{\text{YBCO}}$ ), which was grown epitaxially on a  $\text{SrTiO}_3$  (STO) substrate (see Methods). To prevent degradation of the superconducting properties of the YBCO, the films were covered with a protective capping layer (thickness  $d_{\text{cap}}$ ). Two samples were studied (denoted ‘A’ and ‘B’), with  $d_{\text{YBCO}} = 100$  nm (150 nm) and  $d_{\text{cap}} = 60$  nm (20 nm), respectively (table in Fig. 2a). The samples were mounted close to a stripline for microwave (MW) delivery for NV spin manipulation and a heater for temperature control. A gold bonding wire was placed within a few micrometres of the sample, and was connected to the microwave leads for ESR driving. To nucleate the vortices we field-cooled the samples from a temperature  $T > T_c$  to the system base temperature in an external magnetic field ( $B_z^{\text{f.c.}} = 0.4$  mT), which we applied normal to the sample surface.

To image the resulting vortex distribution, we first obtained a large-area isomagnetic field image using a scanning NV magnetometer. To this end, we fixed the microwave driving frequency  $\nu_{\text{MW}}$  to the zero-field NV-ESR frequency of  $\nu_{\text{ESR}} = 2.87$  GHz and scanned the sample below the stationary NV, the fluorescence of which was constantly interrogated. Whenever a vortex was scanned below the NV, the vortex stray magnetic field shifted  $\nu_{\text{ESR}}$  away from  $\nu_{\text{MW}}$ , resulting in an increase in the NV fluorescence rate. Bright spots in Fig. 2b therefore signal the presence of individual vortices in the sample. Given the cooling field of  $B_z^{\text{f.c.}} = 0.4$  mT and the magnetic flux-quantum  $\Phi_0 = h/2e = 2.07$  mT  $\mu\text{m}^2$  (where  $h$  is Planck’s constant and  $e$  is the electron charge), one expects a

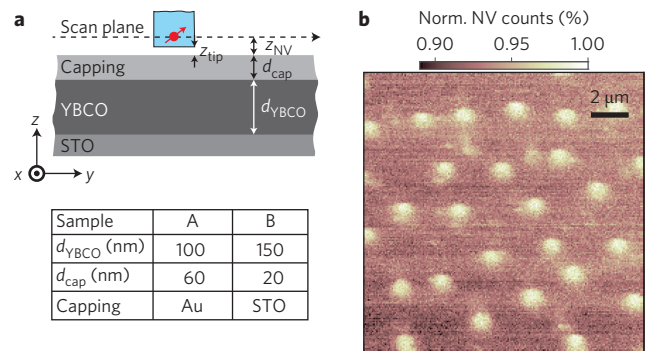


**Figure 2 | Ensemble vortex imaging and sample design.** **a**, Layout of sample and scanning NV sensor. The superconducting YBCO film (thickness  $d_{\text{YBCO}}$ ) was grown on an STO substrate (see text and Methods) and covered by a protective layer (thickness  $d_{\text{cap}}$ ). Key parameters for samples A and B are summarized in the table. The red arrow and blue structure indicate the NV spin and diamond nanopillar, respectively, at distances  $z_{\text{NV}}$  and  $z_{\text{tip}}$  from the sample surface. **b**, Isomagnetic field image of an ensemble of vortices in sample A imaged at  $B = 0$  after field-cooling in  $B_z^{\text{f.c.}} = 0.4$  mT. The microwave driving frequency  $\nu_{\text{MW}}$  was fixed to the zero-field NV ESR at 2.87 GHz, and NV fluorescence was monitored while scanning the sample. Bright areas indicate regions where the NV Zeeman shift exceeds the ESR half linewidth of 6 MHz, that is, where  $B_{\text{NV}} > 0.22$  mT.

vortex density of  $B_z^{\text{f.c.}}/\Phi_0 = 0.19 \mu\text{m}^{-2}$ , that is, 43 vortices in the scan range of  $15 \mu\text{m} \times 15 \mu\text{m}$ , in fair agreement with the 27 vortices observed in Fig. 2.

Further insight into individual vortices can be gained by full, quantitative mapping of the magnetic stray field emerging from a single vortex, which we performed on sample A. We focused on a spatially isolated vortex and conducted a scan with our NV magnetometer, and obtained  $B_{\text{NV}}$  by measuring the Zeeman splitting in optically detected ESR (Fig. 1b) at each pixel of the scan. The vortex was nucleated as before, and imaging was performed in a bias field  $B_{\text{bias}} = 0.45$  mT, which we applied along the  $y$  axis to determine the sign of the measured fields.  $B_{\text{bias}}$  was chosen to be strong enough to induce a sizeable ESR splitting, but weak enough not to generate in-plane vortices in the superconductor. The resulting image (Fig. 3a) yields a map of the projection of the vortex stray field  $\mathbf{B}_{\text{vortex}}(x,y,z)$  onto the NV spin quantization axis,  $\mathbf{e}_{\text{NV}} = (0, \sqrt{2}, 1)/\sqrt{3}$  (which we determined independently before the scan; see Supplementary Section IV). The non-zero angle between  $\mathbf{e}_{\text{NV}}$  and the sample normal  $\mathbf{e}_z$  leads to an asymmetry in the observed stray-field image, which would otherwise be rotationally symmetric in the  $x$ - $y$  plane. (Note that, due to strong twinning in our thin-film sample, the in-plane London penetration depth  $\lambda_L$  is essentially isotropic.) Our quantitative image allows us to directly determine the magnetic flux enclosed by the vortex in the scanning range,  $\Phi_{\text{B,meas}} \approx 0.79$  mT  $\mu\text{m}^2$ , by spatial integration of the data in Fig. 3a. This value is consistent with the vortex carrying a total flux of  $\Phi_0$ , where we would expect a measured flux of  $\Phi_0/\eta \approx 0.83$  mT  $\mu\text{m}^2$ , where  $\eta \approx 2.49$  is a numerically derived correction factor originating from the finite area covered by the scan (Supplementary Section III).

The outstanding stability of our cryogenic NV magnetometer further allowed us to perform a full, three-dimensional mapping of  $\mathbf{e}_{\text{NV}} \cdot \mathbf{B}_{\text{vortex}}(x,y,z)$ . To that end, we scanned the sample at well-defined distances of  $z_{\text{tip}} = 50$  and 100 nm from the diamond tip. The resulting slices of  $\mathbf{B}_{\text{vortex}}(x,y,z = z_{\text{NV}})$  (Fig. 3b), together with an independently measured map of  $\mathbf{B}_{\text{vortex}}(x,y,z)$  along an  $x$ - $z$  plane (Fig. 3c), provide complete, quantitative information about the stray magnetic field emerging from the vortex. Importantly, our data show variations in  $\mathbf{B}_{\text{vortex}}(x,y,z)$  down to the smallest values of  $z$  (where  $z_{\text{tip}} \approx 0$ ), which provides evidence that our imaging is not

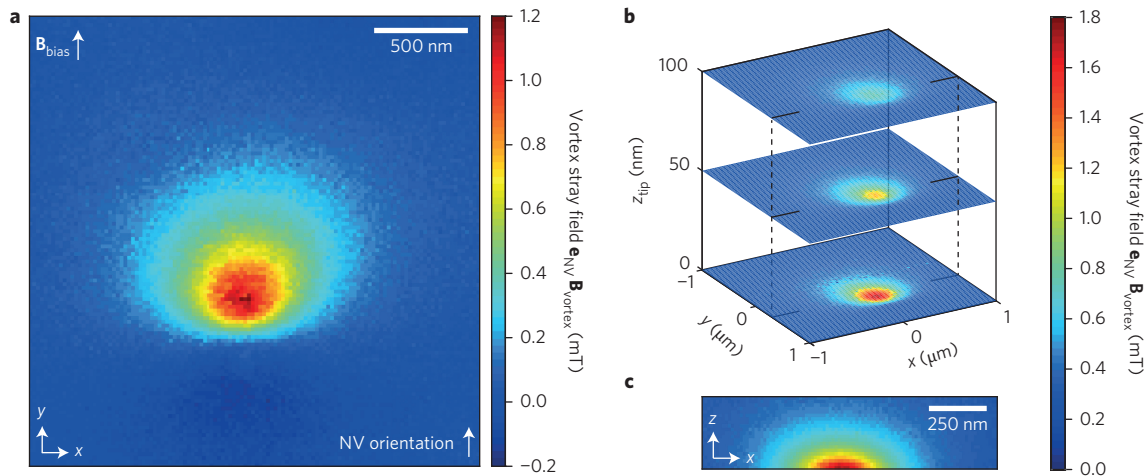


**Figure 3 | Quantitative mapping of single-vortex stray magnetic fields.** **a**, Image of the magnetic stray field from a single vortex in sample A obtained with the NV magnetometer in AFM contact. The stray-field projection onto the NV axis was obtained by measuring Zeeman splitting in the optically detected ESR (Fig. 1b) at each of the  $120 \times 120$  pixels of the scan. The width of the observed vortex stray field is set by  $\Lambda$  (the Pearl length), which is much bigger than our estimated spatial resolution of 10 nm (see main text). **b**, Three-dimensional reconstruction of  $B_{\text{NV}}$  obtained as in **a**, with a different diamond tip. Scans were performed at two out-of-contact heights of 50 and 100 nm, as indicated. **c**, Vertical scan through the vortex stray field in the  $x$ - $z$  plane indicated in **b**.

limited by the size of the detector. In fact, our magnetometer can detect changes in  $\mathbf{B}_{\text{vortex}}(x,y,z)$  with a resolution determined by the spatial extent of the NV's electronic wavefunction, that is, on length scales of  $<1$  nm. As a result, our imaging resolution for magnetic textures on a sample surface is set by  $z_{\text{NV}}$  (the NV-surface distance, Fig. 2a), which in contact is  $\sim 10$  nm (ref. 21; also see below). For the present sample, the distance between NV and superconductor is further increased due to the capping layer to  $\sim 30$  nm.

A central distinguishing feature of NV magnetometry is its ability to provide quantitative measures of magnetic fields on the nanoscale. Here, this feature allows us to test and discriminate existing models for vortex stray fields and to determine the local properties of our superconducting sample. We conducted separate, high-resolution line-scans of  $\mathbf{B}_{\text{vortex}}(x,y,z)$  along the symmetry axes of an individual vortex (nucleated by field cooling in  $B_z^{\text{c}} = 0.2$  mT) in sample B. The resulting measurements of  $\mathbf{B}_{\text{vortex}}(x)$  and  $\mathbf{B}_{\text{vortex}}(y)$  (Fig. 4a,b, respectively) form the basis for our subsequent, quantitative analysis.

The spatial evolution of  $\mathbf{B}_{\text{vortex}}$  is given by the distribution of supercurrents encircling the vortex in the plane of the superconductor. By virtue of the Meissner effect, the field lines generated by these supercurrent loops cannot close in the plane of the superconductor away from the vortex, and  $\mathbf{B}_{\text{vortex}}$  therefore has to resemble a monopole far from the superconductor. A detailed analysis of this vortex far field yields a virtual magnetic monopole of strength  $2\Phi_0$ , located a distance  $\lambda_L$  below the superconductor surface<sup>12,13,22</sup>. Although widely used in the literature, this monopole approximation has the drawback that it does not allow an independent determination of  $\lambda_L$  and  $z_{\text{NV}}$  (that is, changes in  $\lambda_L$  cannot be distinguished from changes in  $z_{\text{NV}}$ ), and that it breaks down for  $z_{\text{NV}} \ll \Lambda$ , where  $\Lambda = 2\lambda_L^2/d_{\text{YBCO}}$  is the Pearl length. Indeed, in our attempts to fit the data (keeping  $\mathbf{e}_{\text{NV}}$  and  $\Phi_0$  fixed and varying the vortex position), the monopole failed to yield a satisfactory fit (Fig. 4a,b, green dashed lines). This discrepancy is a consequence of the close proximity of the NV to the sample and is an opportunity to test the validity of more refined models for vortex stray fields.

A more accurate description of the vortex stray field is offered by Pearl's approach<sup>13,22</sup> to obtain the distribution of superconducting currents (and thereby the stray magnetic field) around vortices in thin-film superconductors. The resulting fit of this Pearl-vortex stray field to our data (Fig. 4a,b, blue lines) indeed shows excellent quantitative agreement. Importantly, and in contrast to the monopole approximation, this fit, paired with the high signal-to-noise

ratio of our data, allows us to independently determine  $\lambda_L$  and  $h_{\text{NV}}$ , the vertical distance between the NV and the Pearl vortex at the centre of the YBCO film. To our knowledge, this is the first time such an independent determination of these quantities has been done in a vortex imaging experiment<sup>12,14,15</sup>. From the fit (Supplementary Section III), we find  $\Lambda = 840 \pm 20$  nm and  $h_{\text{NV}} = 104 \pm 2$  nm. Here,  $h_{\text{NV}}$  is related to the net NV-to-sample standoff distance  $z_{\text{NV}} = h_{\text{NV}} - d_{\text{YBCO}}/2 - d_{\text{cap}} = 9 \pm 3.5$  nm. For samples without a capping layer,  $z_{\text{NV}}$  thus represents the ultimate imaging resolution we can currently achieve with our magnetometer. Our measurement of  $\Lambda$  yields a bulk penetration depth of  $\lambda_L = 251 \pm 14$  nm, which is consistent with previously reported values<sup>12,23</sup> and provides proof of the validity of our model and method.

The analysis of our experimental data provides an example of the great potential the quantitative aspects of NV magnetometry hold for future applications in studying complex condensed-matter systems. Our quantitative fits have allowed us to locally determine the absolute value of  $\lambda_L$ , a quantity that is notoriously hard to measure<sup>6</sup> but of high interest due to its direct link to the structure of the superconducting gap<sup>8</sup>. Furthermore, our analysis has allowed us to draw a clear distinction between two alternative models for vortex stray fields. In analogy, such analysis should in the future allow us to discriminate between competing models for magnetic order in a variety of condensed-matter systems<sup>24,25</sup>. The non-invasiveness of the probe will be a key requirement and warrants discussion of the potential, unwanted heating effects due to NV laser excitation and microwave driving. For YBCO, we repeated vortex imaging with increasing laser powers, and even with the highest values of  $\sim 2$  mW (Supplementary Section VI) we were able to image vortices without observing signs of 'vortex dragging'<sup>12</sup>. For even more fragile samples, there is ample margin to further reduce potential heating effects by using resonant NV laser excitation (requiring nW power levels<sup>26</sup>), all-optical spin manipulation<sup>27</sup> to eliminate microwaves, or pulsed ESR detection<sup>28</sup> with projected laser duty cycles of  $<1\%$  for the longest reported NV coherence times<sup>29</sup>. The resulting, sub-nW average heating powers we project compare favourably to established approaches to studying strongly correlated electron systems<sup>25</sup> at ultralow temperatures.

In conclusion, we have presented the first demonstration of a scanning NV magnetometer operating under cryogenic conditions. We have combined nanoscale spatial resolution and quantitative,

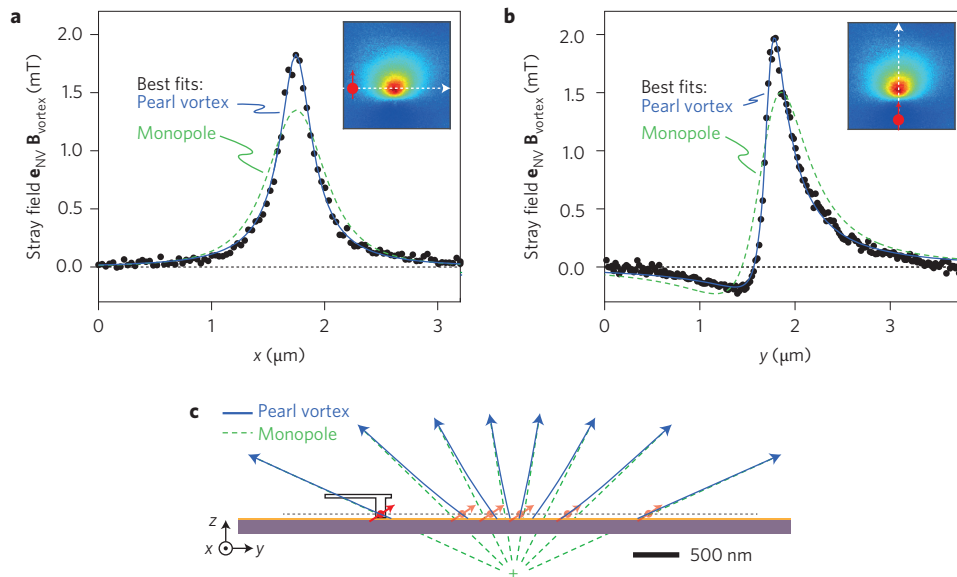


**Figure 4 | Quantitative stray-field analysis and determination of London penetration depth.** **a,b**, High-resolution measurements of the vortex stray field ( $\mathbf{e}_{\text{NV}} \cdot \mathbf{B}_{\text{vortex}}$ ) recorded in sample B along the horizontal ( $x$ ) and vertical ( $y$ ) symmetry axes of a single vortex, as shown in the insets. Blue and green dashed lines represent best fits to a Pearl vortex and magnetic monopole, respectively. From the Pearl vortex fit, we determine  $\lambda_L = 251 \pm 14$  nm, the bulk London penetration depth, which cannot be obtained unambiguously using the monopole model. **c**, Vortex magnetic field lines close to the superconductor surface within the monopole (green dashed) and Pearl (blue solid) approximations, illustrating the strong discrepancy between the two models close to the surface ( $z_{\text{NV}} = \lambda_L$ ). In all panels, the red arrow shows the orientation of the NV with respect to the sample.

non-invasive magnetic imaging to map the stray magnetic fields of individual Pearl vortices in superconducting thin films with high sensitivity and spatial resolution. Our results establish NV magnetometry as a powerful tool to address complex, electronic systems through nanoscale magnetic-field imaging. Specifically, our NV magnetometer could in the future be used to address the elusive pseudogap phase<sup>5,30</sup> of high- $T_c$  superconductors or inhomogeneous superconductors at the nanoscale<sup>31</sup>. Both problems are largely inaccessible to present-day nanoscale sensing technologies due to a lack of spatial resolution or sensitivity or the ability to operate at elevated temperatures. Further extending our measurement capabilities through spin relaxometry<sup>32</sup> or quantum sensing based on dynamical decoupling<sup>33</sup> is another exciting avenue that would drastically enhance the dynamic range of our sensor and therefore yield access to the nontrivial dynamical properties of individual vortices<sup>34</sup>. The resulting projected dynamical range and sensitivity, together with the spatial resolution and quantitative aspects demonstrated here, will open the door to studying unexplored aspects of quantum matter far beyond the applications in superconductivity<sup>24,35</sup> demonstrated here.

*Note added in proof:* During completion of this work, we became aware of related results on cryogenic NV magnetometry<sup>36</sup>.

## Methods

Methods and any associated references are available in the [online version of the paper](#).

Received 7 November 2015; accepted 16 March 2016; published online 2 May 2016

## References

- Essmann, U. & Träuble, H. The direct observation of individual flux lines in type II superconductors. *Phys. Lett. A* **24**, 526–527 (1967).
- Bending, S. J. Local magnetic probes of superconductors. *Adv. Phys.* **48**, 449–535 (1999).
- Hess, H. F., Robinson, R. B., Dynes, R. C., Valles, J. M. & Waszczak, J. V. Scanning-tunneling-microscope observation of the Abrikosov flux lattice and the density of states near and inside a fluxoid. *Phys. Rev. Lett.* **62**, 214 (1989).

- Hoffman, J. E. *et al.* A four unit cell periodic pattern of quasi-particle states surrounding vortex cores in  $\text{Bi}_2\text{Sr}_2\text{CaCu}_2\text{O}_{8+\delta}$ . *Science* **295**, 466 (2002).
- Fischer, O., Kugler, M., Maggio-Aprile, I., Berthod, C. & Renner, C. Scanning tunneling spectroscopy of high-temperature superconductors. *Rev. Mod. Phys.* **79**, 353 (2007).
- Luan, L. *et al.* Local measurement of the penetration depth in the pnictide superconductor  $\text{Ba}(\text{Fe}_{0.95}\text{Co}_{0.05})_2\text{As}_2$ . *Phys. Rev. B* **81**, 100501 (2010).
- Kirtley, J. R. *et al.* Scanning squid susceptometry of a paramagnetic superconductor. *Phys. Rev. B* **85**, 224518 (2012).
- Hardy, W. N., Bonn, D. A., Morgan, D. C., Liang, R. & Zhang, K. Precision measurements of the temperature dependence of  $\lambda$  in  $\text{YBa}_2\text{Cu}_3\text{O}_{6.95}$ : strong evidence for nodes in the gap function. *Phys. Rev. Lett.* **70**, 3999 (1993).
- Rondin, L. *et al.* Nanoscale magnetic field mapping with a single spin scanning probe magnetometer. *Appl. Phys. Lett.* **100**, 153118 (2012).
- Tetienne, J. P. *et al.* The nature of domain walls in ultrathin ferromagnets revealed by scanning nanomagnetometry. *Nature Commun.* **6**, 6733 (2014).
- Maletinsky, P. *et al.* A robust scanning diamond sensor for nanoscale imaging with single nitrogen-vacancy centres. *Nature Nanotech.* **7**, 320–324 (2012).
- Auslaender, O. M. *et al.* Mechanics of individual isolated vortices in a cuprate superconductor. *Nature Phys.* **5**, 35–39 (2008).
- Pearl, J. Current distribution in superconducting films carrying quantized fluxoids. *Appl. Phys. Lett.* **5**, 65 (1964).
- Tafari, F., Kirtley, J. R., Medaglia, P. G., Orgiani, P. & Balestrino, G. Magnetic imaging of pearl vortices in artificially layered  $(\text{Ba}_{0.9}\text{Nd}_{0.1}\text{CuO}_{2+x})_m/(\text{CaCuO}_2)_n$  systems. *Phys. Rev. Lett.* **92**, 157006 (2004).
- Vasyukov, D. *et al.* A scanning superconducting quantum interference device with single electron spin sensitivity. *Nature Nanotech.* **8**, 639–644 (2013).
- Taylor, J. *et al.* High-sensitivity diamond magnetometer with nanoscale resolution. *Nature Phys.* **4**, 810–816 (2008).
- Balasubramanian, G. *et al.* Nanoscale imaging magnetometry with diamond spins under ambient conditions. *Nature* **455**, 648–651 (2008).
- Rondin, L. *et al.* Magnetometry with nitrogen-vacancy defects in diamond. *Rep. Prog. Phys.* **77**, 056503 (2014).
- Bouchard, L. S., Acosta, V. M., Bauch, E. & Budker, D. Detection of the Meissner effect with a diamond magnetometer. *New J. Phys.* **13**, 025017 (2011).
- Schaefer-Nolte, E., Reinhard, F., Ternes, M., Wrachtrup, J. & Kern, K. A diamond-based scanning probe spin sensor operating at low temperature in ultra-high vacuum. *Rev. Sci. Instrum.* **85**, 013701 (2014).
- Appel, P., Ganzhorn, M., Neu, E. & Maletinsky, P. Nanoscale microwave imaging with a single electron spin in diamond. *New J. Phys.* **17**, 112001 (2015).
- Carneiro, G. & Brandt, E. H. Vortex lines in films: fields and interactions. *Phys. Rev. B* **61**, 6370 (2000).
- Wölbling, R. *et al.* Optimizing the spin sensitivity of grain boundary junction nanosquids—towards detection of small spin systems with single-spin resolution. *Supercond. Sci. Technol.* **27**, 125007 (2014).

24. Young, A. F. *et al.* Spin and valley quantum Hall ferromagnetism in graphene. *Nature Phys.* **8**, 550–556 (2012).
25. Xia, J., Maeno, Y., Beyersdorf, P., Fejer, M. & Kapitulnik, A. High resolution polar Kerr effect measurements of  $\text{Sr}_2\text{RuO}_4$ : evidence for broken time-reversal symmetry in the superconducting state. *Phys. Rev. Lett.* **97**, 167002 (2006).
26. Robledo, L. *et al.* High-fidelity projective read-out of a solid-state spin quantum register. *Nature* **477**, 574–578 (2011).
27. Yale, C. G. *et al.* All-optical control of a solid-state spin using coherent dark states. *Proc. Natl Acad. Sci. USA* **110**, 7595–7600 (2013).
28. Dréau, A. *et al.* Avoiding power broadening in optically detected magnetic resonance of single NV defects for enhanced DC magnetic field sensitivity. *Phys. Rev. B* **84**, 195204 (2011).
29. Balasubramanian, G. *et al.* Ultralong spin coherence time in isotopically engineered diamond. *Nature Mater.* **8**, 383–387 (2009).
30. Timusk, T. & Statt, B. The pseudogap in high-temperature superconductors: an experimental survey. *Rep. Prog. Phys.* **62**, 61–122 (1999).
31. Kresin, V. Z., Ovchinnikov, Y. N. & Wolf, S. A. Inhomogeneous superconductivity and the ‘pseudogap’ state of novel superconductors. *Phys. Rep.* **431**, 231–259 (2006).
32. Kolkowitz, S. *et al.* Probing Johnson noise and ballistic transport in normal metals with a single-spin qubit. *Science* **347**, 1129–1132 (2015).
33. De Lange, G., Risté, D., Dobrovitski, V. V. & Hanson, R. Single-spin magnetometry with multipulse sensing sequences. *Phys. Rev. Lett.* **106**, 080802 (2011).
34. Embon, L. *et al.* Probing dynamics and pinning of single vortices in superconductors at nanometer scales. *Sci. Rep.* **5**, 7598 (2015).
35. Levitov, L. & Falkovich, G. Electron viscosity, current vortices and negative nonlocal resistance in graphene. *Nature Phys.* <http://dx.doi.org/10.1038/nphys3667> (2016).
36. Pelliccione, M. *et al.* Scanned probe imaging of nanoscale magnetism at cryogenic temperatures with a single-spin quantum sensor. Preprint at <http://arXiv.org/abs/1510.02780> (2015).

### Acknowledgements

The authors thank V. Jacques, A. Högele and S.D. Huber for discussions and feedback on the manuscript. The authors acknowledge Attocube Systems for support and the joint development of the microscope system used here. The authors also acknowledge financial support from SNI (NCCR QSIT), SNF grants 143697 and 155845, and EU FP7 grant 611143 (DIADEMS).

### Author contributions

L.T., D.R. and M.G. carried out the experiment and analysed the data. E.N., P.A. and M.G. fabricated scanning probe tips. B.M., R.K. and D.K. grew the YBCO samples and provided valuable input for the experiment. All authors commented on the manuscript. P.M. wrote the manuscript, conceived the experiment and supervised the project.

### Additional information

Supplementary information is available in the [online version of the paper](#). Reprints and permissions information is available online at [www.nature.com/reprints](http://www.nature.com/reprints). Correspondence and requests for materials should be addressed to P.M.

### Competing financial interests

The authors declare no competing financial interests.

## Methods

**Sample fabrication.** Epitaxially grown *c*-axis-oriented YBCO thin films on STO single-crystal (001)-oriented substrates were fabricated by pulsed laser deposition (PLD), followed either by *in situ* electron-beam evaporation of Au at room temperature (sample A) or by *in situ* epitaxial growth of an STO cap layer via PLD (sample B). For details on the PLD growth of our YBCO films on STO substrates and their structural and electric transport properties, see refs 37 and 38. In brief, our YBCO films typically yield a  $0.1^\circ$  full-width at half-maximum of the rocking curve at the (005) X-ray diffraction peak, have an inductively measured transition temperature of  $T_c = 89$  K and normal-state resistivity of  $\rho \approx 50 \mu\Omega \text{ cm}$  at  $T = 100$  K.

The thicknesses of the samples were determined by *in situ* high-pressure reflection high-energy electron diffraction for both the YBCO and STO films. Using the *c*-axis lattice parameters, measured using X-ray diffraction, we then obtained the thicknesses for the YBCO and STO films as given in the main text. The Au growth rate was determined using a quartz-crystal monitor. For all the layers, we estimated the error in determining their thicknesses to be 2–3%.

**Experimental set-up.** The experimental set-up was based on a low-temperature, tuning-fork-based AFM (Attocube, attoLIQUID 1000). The microscope was housed in a low-vibration, nitrogen-free liquid  $^4\text{He}$  bath cryostat with a base temperature of 4.2 K, which was equipped with a three-dimensional vector magnet (0.5 T in all directions, Janis). Optical access to the AFM tip was provided by an achromatic, low-temperature-compatible objective (Attocube LT-APO/VISIR/0.82, 0.82 NA) and a home-built confocal microscope, directly mounted on top of the cryostat. The

microscope head (including the sample, the diamond tip and the objective) was located in a housing filled with  $^4\text{He}$  buffer gas. The housing was directly immersed in the liquid  $^4\text{He}$  bath. The diamond tip was attached to a tuning fork for force feedback in the AFM, which was provided by commercial electronics (Attocube, ASC500). Two separate positioning units (Attocube, an ANSxyz50 on top of an ANPxyz51) provided individual high-accuracy positioning for both the sample and sensor. Temperature control of the sample above 4.2 K was provided by a resistive heater (IMS, ND3-1206EW1000G) and a temperature controller (LakeShore, Model 355). Excitation light for NV fluorescence was provided by a solid-state laser at 532 nm (LaserQuantum, GEM532). Red fluorescence photons were coupled into a single-mode fibre guided to an avalanche photodiode for counting (Excelitas, SPCM-ARQH-13). Data acquisition and scan control were achieved using a digital acquisition card (National Instruments, NI-6602 and NI-6733) and Matlab-based experiment control software. Microwave signals for spin manipulation were generated by a signal generator (Rohde & Schwarz, SMB100A), amplified (Minicircuit, ZHL-42W+) and delivered to the NV centre using a gold wire (diameter of 25  $\mu\text{m}$ ) positioned across the sample.

## References

37. Werner, R. *et al.*  $\text{YBa}_2\text{Cu}_3\text{O}_7/\text{La}_{0.7}\text{Ca}_{0.3}\text{MnO}_3$  bilayers: interface coupling and electric transport properties. *Phys. Rev. B* **82**, 224509 (2010).
38. Scharinger, S. *et al.* Magnetic field dependence of the critical current in  $\text{YBa}_2\text{Cu}_3\text{O}_{7-\delta}/\text{Au}/\text{Nb}$  ramp-zigzag Josephson junctions. *Phys. Rev. B* **86**, 144531 (2012).